

Evolution of Galaxy Luminosity Function Using Photometric Redshifts

B. H. F. Ramos^{1,2}, P. S. Pellegrini^{1,2}, C. Benoist^{3,2}, L. N. da Costa^{1,2}, M. A. G. Maia^{1,2}, M. Makler^{4,2}, R. L. C. Ogando^{1,2}, F. de Simoni^{1,2}, A. A. Mesquita⁵

ABSTRACT

We examine the impact of using photometric redshifts for studying the evolution of both the global galaxy luminosity function (LF) and that for different galaxy types. To this end we compare the LFs obtained using photometric redshifts from the CFHT Legacy Survey (CFHTLS) D1 field with those from the spectroscopic survey VIMOS VLT Deep Survey (VVDS) comprising ≈ 4800 galaxies. We find that for $z \leq 2.0$, in the interval of magnitudes considered by this survey, the LFs obtained using photometric and spectroscopic redshifts show a remarkable agreement. This good agreement led us to use all of the four Deep fields of the CFHTLS comprising ≈ 386000 galaxies to compute the LF of the combined fields and estimate directly the error in the parameters based on the field-to-field variation. We find that the characteristic absolute magnitude M^* of Schechter fits fades by ≈ 0.7 mag from $z \approx 1.8$ to $z \approx 0.3$, while the characteristic density ϕ^* increases by a factor of ≈ 4 in the same redshift interval. We use the galaxy classification provided by the template fitting program used to compute photometric redshifts and split the sample into galaxy types. We find that these Schechter parameters evolve differently for each galaxy type, an indication that their evolution is a combination of several effects: galaxy merging, star formation quenching and mass assembly. All these results are compatible with those obtained by different spectroscopic surveys such as VVDS, DEEP2 and zCosmos, which reinforces the fact that photometric redshifts can be used to study galaxy evolution, at least for the redshift bins adopted so far. This is of great interest since future very large imaging surveys containing hundreds of millions of galaxies will allow to obtain important precise measurements to constrain the evolution of the LF and to explore the dependence of this evolution on morphology and/or color helping constrain the mechanisms of galaxy evolution.

¹Observatório Nacional, Rua Gal. José Cristino 77, Rio de Janeiro, RJ - 20921-400, Brazil; ramos@linea.gov.br, pssp@linea.gov.br, ldacosta@linea.gov.br, maia@linea.gov.br, ogando@linea.gov.br, fsimoni@linea.gov.br

²Laboratório Interinstitucional de e-Astronomia - LIneA, Rua Gal. José Cristino 77, Rio de Janeiro, RJ - 20921-400, Brazil

³Université de Nice Sophia-Antipolis, CNRS, Observatoire de la Côte d'Azur, UMR 6202 CASSIOPEE, BP 4229, F-06304 Nice Cedex 4, France; benoist@oca.eu

⁴Centro Brasileiro de Pesquisas Físicas, Rua Dr. Xavier Sigaud, 150, Rio de Janeiro 22290-180 RJ, Brazil; martin@cbpf.br

⁵Universidade Federal do Rio de Janeiro, Observatório do Valongo, Ladeira do Pedro Antonio, 43, Rio de Janeiro 20080-090, RJ, Brazil; albertoalves@on.br

Subject headings: galaxies: evolution — galaxies: luminosity function

1. Introduction

The galaxy luminosity function, or number density of galaxies as a function of their luminosity, is a fundamental property of the galaxy distribution, as it provides information on how visible matter is distributed among galaxies of various luminosities at a given epoch. Therefore, its evolution can be used to constrain models of galaxy evolution and structure formation (Benson et al. 2003). In order to set tight constraints on these models, one would ideally divide galaxies into a variety of subgroups and derive independent luminosity functions that are known to vary significantly with respect to several physical parameters such as redshift, color, galaxy type, star formation rate, etc. With the advent of very large and deep galaxy surveys, this has become possible, leading to a large number of works (e.g., Faber et al. 2007; Christlein et al. 2009; Zucca et al. 2009). However, in order to benefit from large, homogeneous and complete samples, in most cases one has to rely only on the photometric information with at most a partial spectroscopic coverage.

While the local luminosity function has been extensively studied due to numerous spectroscopic surveys carried out over the years (Marzke et al. 1994; Marzke & da Costa 1997; Marzke et al. 1998; Folkes et al. 1999; Blanton et al. 2001; Madgwick et al. 2002), probing its evolution to high redshifts still represents a challenge. One possible way of doing that is to take advantage of the recent multi-band photometric surveys, such as the Canada-France-Hawaii Telescope Legacy Survey (CFHTLS), and use the photometric redshift technique to estimate distances. The purpose of this paper is to show that this is in fact possible, at least using the redshift bins here adopted, yielding reliable results. This is demonstrated using the VIMOS VLT Deep Survey (VVDS) data and one of the Deep fields of CFHTLS. Based on this finding we use all CFHTLS Deep fields to compute a combined luminosity function and estimate the cosmic variance on their fitted Schechter parameters at different redshifts. Finally, we use the information provided by the template fitting routine used to estimate the photometric redshift to split the sample into galaxy types, and compare with the few results available in the literature. This is relevant to investigate how reliable this approach can be to explore the data that will eventually become public for surveys such as the Dark Energy Survey (DES) and Large Synoptic Survey Telescope (LSST).

In Section 2 of this paper, the details on the method used to compute the luminosity function are discussed. The data used is briefly described in Section 3. In Section 4, the results of the comparison of the luminosity functions computed using spectroscopic and photometric redshifts are presented. In this section we also show the evolution of the luminosity function derived for the combined sample comprising all galaxies and split into different galaxy types, which are then compared with the results of other authors. We present a summary of our conclusions in Section 5.

Throughout this paper, the cosmology used is $\Omega_m = 0.3$, $\Omega_\lambda = 0.7$ and results are expressed in terms of $h = H_0/100$.

2. Estimating the Luminosity Function

The luminosity function $\phi(M)dM$, expressing the number of galaxies with absolute magnitudes in the interval M and $M+dM$ per unit volume, is calculated in intervals of redshift using the $1/V_{max}$ method (Schmidt 1968). Thus a galaxy of absolute magnitude M at redshift z contributes to the luminosity function with weight $1/V_{max}$, where V_{max} is the maximum volume within which the galaxy apparent magnitude is found between the catalog apparent magnitude limits (also bounded by the redshift bin limits).

The absolute magnitudes are calculated as:

$$M = m - 25 - 5\log(D_L) - K \quad (1)$$

where m is the apparent magnitude of the galaxy; the luminosity distance is given by $D_L = (1+z)r$, where r is the comoving distance in $h^{-1}Mpc$; K is the K -correction for the shift of the observed spectrum with relation to rest frame reference band wavelength and width. In this work we deal only with the i' -band in the AB photometric system, so M stands for $M_{i',AB}$ and no correction for intrinsic dust reddening was performed.

Our source for K -corrections is the code Le Phare, which was run with spectral energy distributions (SEDs) from Coleman et al. (1980) with the addition of 8 SEDs from Kinney et al. (1996) (Ilbert et al. 2006). These K -corrections are shown in Figure 1, and they are calculated for each galaxy based on the best fitting SED.

In the following analysis, we fit the usual Schechter (1976) function:

$$\Phi(M)dM = 0.4 \ln 10 \phi^* 10^{0.4(\alpha+1)(M^*-M)} \times e^{-10^{0.4(M^*-M)}} dM \quad (2)$$

where M^* is the characteristic absolute magnitude and ϕ^* is the normalization factor. Fits for the Schechter function were performed by a least square method using the Marquardt-Levenberg algorithm with M^* , ϕ^* and α as free parameters.

3. Data

In this work, we used photometric data from the four Deep fields of the CFHTLS from observations made with the MegaCam camera at the CFHT. Each field (D1, D2, D3 and D4) covers ≈ 1 square degree and was observed in the u^* , g' , r' , i' , and z' bands (Table 1 presents general information).

The CFHTLS-D1 field is particularly interesting for this work since it has both photometric and spectroscopic observations from VVDS. Photometry in the VVDS was carried out using B , V ,

R , I filters (Ilbert et al. 2006) and additional photometric data in the J and K bands are available from Iovino et al. (2005). The spectra were obtained with the VIMOS spectrograph at the VLT, for objects selected in the range $17.5 \leq I_{AB} \leq 24.0$ (Le Fèvre et al. 2005), yielding a total of 6582 galaxies. We used only good quality spectroscopic redshifts (quality flags 2, 3 and 4), to $z = 2$, reducing the sample to 4813.

In this analysis, we used the color catalogs processed by Terapix¹ for all four Deep Fields (version T0003), but with a different set of updated masks produced by one of the authors (C.B.) to cover defective regions and those surrounding very bright stars. This was performed in two steps: first by creating automatic polygons centered on stars brighter than $i=19.0$ with a shape including diffraction spikes and a size scaled to the star magnitudes; second by correcting by hand these polygons in the case of the brightest stars that show large ghosts and by adding polygons to mask remaining defects such as satellite trails. From these catalogs, we selected only objects classified as galaxies by the Terapix group, from a morphological criterion based on their location in a compactness (radius containing 50% of the total flux) -magnitude distribution (see Terapix site¹), and located outside masked regions, in order to avoid objects with contaminated magnitudes. The photometric redshifts we use are those provided in these catalogs, calculated by the Le Phare code, which is based on a template fitting method and improved by an empirical training set, which reduces the dispersion $\sigma_{|\delta|z/(1+z)}$ from 0.047 to 0.029. Only galaxies with available magnitudes in at least three bands had photometric redshifts determined. The process to calculate such redshifts is described in detail in Ilbert et al. (2006) and was conducted by the Terapix and VVDS teams.

We choose the i' band as the one defining the samples in this work, since it is the closest to that (I -band) defining the VVDS sample. Comparing i'_{AB} (CFHTLS) and I_{AB} (VVDS) magnitudes down to $i'_{AB} = 24$ and $z < 1.3$ we find $i'_{AB} = I_{AB} - 0.11 \pm 0.16$. Due to this small difference, we took for the i' band the same values for the magnitude limit as the one in the I -band. Thus, whenever we analyzed data from the CFHTLS individual fields (and specially to compare the results with the VVDS survey) we used the limits $17.5 \leq i'_{AB} \leq 24.0$, also restraining the analysis to $z \leq 2.0$. When analyzing the sample from the combination of the four CFHTLS areas, we extended these limits to $17.5 \leq i'_{AB} \leq 25.0$, corresponding to a 80% completeness level (Ilbert et al. 2005).

For a sample with magnitude limit of $i'_{AB} = 24$ (as in this work), it is still possible to probe the faint end of the luminosity function at $z \approx 1$ and determine a reliable value for α when fitting the Schechter function. Due to the lack of good sampling of faint objects at higher redshifts, we fix the value of α , usually for $z > 1.0$, to that obtained in a previous bin where α is more reliably determined.

In the analysis of the following sections, we subdivide the samples in individual CFHTLS fields in redshift intervals [0.05-0.2], [0.2-0.4], [0.4-0.6], [0.6-0.8], [0.8-1.0], [1.0-1.3] and [1.3-2.0] as used by Ilbert et al. (2005). When analyzing the combined sample of four fields, the last intervals

¹<http://terapix.iap.fr/>

considered are [1.3-1.6] and [1.6-2.0]. Table 2 presents the number of galaxies in each redshift bin for each sample analyzed in this work.

We discard galaxies with large i-band magnitude errors (>0.30 mag) and photometric redshift errors ($\epsilon_z > 0.5z$). This process discards 30% of the galaxies in the redshift bin [0.05-0.2], less than 1% in the bin [0.2-0.4] and a negligible amount in more distant bins. The total number of galaxies in the four CFHTLS Deep fields resulting from all these selections mentioned above is 385910 objects.

4. Results

4.1. Photometric versus Spectroscopic Redshifts

In order to check how well photometric redshifts reproduce the luminosity function obtained with spectroscopic redshifts, we selected a sample of galaxies from the CFHTLS-D1 field in common with the VVDS area, with both spectroscopic and photometric redshift determinations. We call this data the Spectroscopic Sample. We note that photometric redshifts for field D1 were obtained in the CFHTLS from all available magnitudes which means that for many galaxies of this Spectroscopic Sample typically 5 to 9 filters were used.

Luminosity functions were calculated in different redshift intervals and Schechter fits were obtained. The derived M^* and ϕ^* are presented in Table 3 (results obtained using both spectroscopic (z_{spec}) and photometric (z_{phot}) redshifts), while the luminosity functions and their Schechter fits are shown in Figure 2. We note that these functions are not representative of a fair galaxy sample since we do not apply the corrections for sampling biases and redshift determination efficiency rate as described by Ilbert et al. (2005). Nevertheless, since our primary goal is to compare luminosity functions derived with z_{phot} and z_{spec} , for the same set of objects, the fact that both functions are not fair representations is not relevant and they are computed only to evaluate their differences in M^* and ϕ^* . These differences are shown in Figure 3.

At small redshifts ($0.05 < z < 0.2$) the uncertainties are large and might reflect the small number of galaxies in this bin (see Table 2) which prevents a reliable determination of M^* and ϕ^* . At higher redshifts the results show a remarkable agreement indicating that photometric redshifts reproduce the spectroscopic results.

4.2. Combining the CFHTLS Deep Fields

We also calculate the luminosity function for all galaxies in the VVDS area using photometric redshifts and compare the characteristic parameters with those derived spectroscopically by Ilbert et al. (2005) yielding a good agreement between both results. However, as shown below, the

availability of four CFHTLS areas similar in size can be used to improve the statistics concerning this comparison as well as to investigate and quantify the differences due to cosmic variance, at the ≈ 0.7 (effective) square degree scale. Differently from field D1, photometric redshifts for fields D2, D3 and D4 were obtained from the set of filters u^* , g' , r' , i' , and z' . We estimate that for the combined four CFHTLS fields, 76% of the objects had z_{phot} calculated with at least these five filters. Moreover as shown by Ilbert et al. (2006), the inclusion of the BVRIJK magnitudes for galaxies in the CFHTLS-D1 field reduces the number of catastrophic events at $z > 1.3$ (due to the J and K bands) but reduces $\sigma_{|\delta|z/(1+z)}$ from 0.029 to 0.026. As discussed by Ilbert et al. (2006) this is the larger effect of including the additional VVDS filters and the J and K bands. These authors also conclude that the accuracy of the photometric redshifts decreases toward fainter apparent magnitudes and although half of the objects with catastrophic errors are those classified as starburst, the redshift accuracy is approximately independent of type.

The derived luminosity functions and respective Schechter fits for each CFHTLS field are presented in Figure 4 for different redshift bins. Characteristic parameters M^* , ϕ^* and α of Schechter fits are presented in Table 4. Although there is a general good agreement, systematic differences are seen among the fields, showing that cosmic variance is present in samples determined at the 0.7 deg^2 scale. In order to increase the number of objects in each redshift bin and minimize cosmic variance, we merged the samples of the four fields in a single combined CFHTLS sample. The luminosity functions and their Schechter fits in each redshift bin, as well as the magnitude range used for fitting, are shown in Figure 5, while M^* , ϕ^* and α are presented in Table 5.

We note two features from Figure 5. One is that with photometric redshifts it is possible to infer the apparent non-linear shape of the faint end of the luminosity functions seen at redshifts $z < 0.6$. It is tempting to identify an upturn of the function before the incompleteness cut in the closest redshift bins. There is still a lot of discussion in the literature concerning this issue (e.g., Ryan et al. 2007; Liu et al. 2008; Montero-Dorta & Prada 2009; Reddy & Steidel 2009; Bañados et al. 2010; Oesch et al. 2010; Trenti et al. 2010) and it is beyond the scope of this paper to address this question. We briefly mention that some authors such as Blanton et al. (2005) claim the necessity to modify the Schechter function to correctly describe the data, particularly the upturn of the function at faint magnitudes. Anyway, it is becoming clear that this feature is a consequence of a mix of galaxy populations (e.g., Christlein et al. 2009), which at fainter magnitudes are dominated by very late type galaxies. We mention this issue again in the next section.

A second interesting feature is the systematic excess of galaxies at the bright end ($M < -24$), a range which introduces significant uncertainties on the fitted Schechter functions and which were avoided in our fitting process. Indeed the small areas of the individual CFHTLS fields may be subject to a particular larger structure in a given redshift bin. For instance, Guzzo et al. (2007) detected a galaxy cluster at $z = 0.7$ in field D2 that could be the reason for the excess at the bright end displayed by the respective luminosity function in Figure 4. However, the combined luminosity functions in Figure 5 do show the excess for all redshift bins where the bright end is observable. We note that Montero-Dorta & Prada (2009) have also shown this excess in their analysis of the

SDSS-DR6 and claim this is the contribution of galaxies with active nuclei, presenting a luminosity excess compared to normal galaxies.

The evolution of M^* and ϕ^* for the individual fields as well as for the combined sample are shown in Figure 6. The results of the combined area largely agrees with those of Ilbert et al. (2005) for the evolution of both M^* and ϕ^* , as well as with those for the SDSS of Blanton et al. (2001) for the DR1 and Montero-Dorta & Prada (2009) for the DR6. These results indicate for the global sample a slow fading of M^* with cosmic time by ≈ 0.7 mag from $z \approx 1.8$ to $z \approx 0.3$ and a much faster dimming by ≈ 0.8 mag to $z = 0$. Our results are also compatible with those of Faber et al. (2007), who analyzing the DEEP2 and COMBO-17 surveys in the B-band, find a dimming in M^* of 1.2-1.3 mag from $z = 1$ to $z = 0$. Also, Zucca et al. (2009) find that, in the zCOSMOS 10k sample, M^* fades in the B-band by ≈ 0.7 mag from $z \approx 0.9$ to $z \approx 0.2$.

The lower panel of Figure 6 shows for ϕ^* a similar trend as that of M^* with an increase in density by a factor of ≈ 4 from $z \approx 1.8$ to $z \approx 0.3$. The data suggest that there is also a significant increase in the characteristic density of M^* galaxies in the i' -band from $z = 0.3$ to $z = 0$, by a factor of ≈ 2 . We also show in this figure the results of Gabasch et al. (2006) for the i' band, which uses photometric redshifts and essentially indicates no evolution for M^* and ϕ^* .

We note that the plateau seen in the lower panel of Figure 6 in the interval $1.1 > z > 0.5$ is consistent with the decrease of the merging rate shown in Figure 5 of Conselice (2006). Also noticeable in Figure 6 is that, near $z = 0$, M^* dims rapidly, while ϕ^* also rises significantly, with these values at $z=0$ agreeing with those observed in SDSS. This will be addressed in the next section.

Since the errorbars plotted in this figure for the combined area are the variances of M^* and ϕ^* , for the four fields, Figure 6 and Table 4 allow us to estimate that the effect of cosmic variance over M^* is ≈ 0.15 mag for these fields of size ≈ 0.7 square degree for $z < 1$. Similarly, the effect of cosmic variance over ϕ^* from these areas is $\approx 1.20 \times 10^{-3} h^3 \text{gals mag}^{-1} \text{Mpc}^{-3}$.

4.3. Analysis per Galaxy Types

As many authors have pointed out, the shape of the luminosity functions largely depends on the galaxy population mix of the sample under analysis (e.g., Sandage et al. 1985; Blanton et al. 2001; Croton et al. 2005; Faber et al. 2007; Zucca et al. 2009). So, in order to investigate the relative contributions of each galaxy type to the luminosity function evolution, we have the advantage that the CFHTLS catalog includes the best fit SED type that gave rise to the galaxy redshift. This is one of the additional benefits of using a template fitting method to compute photometric redshifts. We stress that although we refer to the galaxy types in this work as E, S, Irr and starburst (sb), they should be considered spectral types instead of morphological ones, since they are attributed as a result of a SED fitting process. Luminosity functions and respective Schechter fits for these types are presented in Table 6 and shown in Figure 7 in different redshift bins for the combined

CFHTLS areas. The combination of the four fields was particularly important in the case of the samples separated per galaxy type, in order for them to be statistically significant.

The galaxies classified here as (Irr+sb) outnumber the E and S types for objects fainter than $M = -20$ at all redshifts and are the dominant class for $z > 1.6$, as can be seen from Figure 7. As noted by Zucca et al. (2006), these galaxies are responsible for most of the evolution (and steepening) of the global luminosity function measured by Ilbert et al. (2005). We also note the rise of the E class at $z \approx 1.6$, forming even at these early epochs the majority of the brightest objects ($M < -22$). As the (Irr+sb)-type, S-type galaxies display in the CFHTLS data a Schechter form at early epochs, in the range $1.6 \leq z \leq 2.0$, but present local deviations at the faint end at $z < 0.8$. Moreover, Figure 7 shows that, as reported by different authors (e.g., Blanton et al. 2005; Christlein et al. 2009), the steepness of the global luminosity function is due to the increasing number of (Irr+sb)-type galaxies with decreasing luminosity. Also, the contribution of the S-type galaxies may play a role in deviating the luminosity function from a linear form at the faint end. We also note that the excess at the bright end at $z > 0.8$ is present in the latter types as clearly seen in the (Irr+sb) luminosity functions.

In Figures 8, 9 and 10 we show the evolution of M^* and ϕ^* for the luminosity functions of types E, S and (Irr+sb) galaxies. We present values with reference to those at $z = 0.5$, termed here M_{ref}^* and ϕ_{ref}^* , in order to compare with different authors. We find that in the i' -band:

- E-galaxies show a mild evolution of M^* , with a dimming of ≈ 0.6 mag from $z \approx 1.5$ to $z = 0.3$ while their number density increases in the same redshift interval by a factor ≈ 3 . We have also considered evolutionary effects using the K -corrections from Annis (2000) derived for the SDSS, and based on the evolutionary synthesis code PEGASE-2 of Fioc & Rocca-Volmerange (1997). Using the K -correction representing passive evolution, we find that it does seem to reproduce reasonably well the 0.6 mag dimming of this type of galaxies, in the redshift range mentioned above;
- S-galaxies undergo a fading in their characteristic value M^* by 1.3 mag from $z \approx 1.8$ to $z = 0.3$ while ϕ^* presents an increase by a factor of at least 2 from $z \approx 1.3$ to $z \approx 0.3$;
- (Irr+sb)-galaxies shows a continuous decrease in brightness ≈ 2 mag in M^* from $z \approx 1.8$ to $z = 0.3$. On the other hand ϕ^* presents a distinctive evolution: it rises by a factor ≈ 4 from $z \approx 1.8$ to $z \approx 1.2$, then proceeds in the reverse sense with a decrease in density by a factor ≈ 1.8 to $z = 0.3$. We note that this galaxy type presents lower accuracies of photometric redshifts determinations as shown in figure 8 of Ilbert et al. (2006);
- Inspection of table 7 indicates that the slope of the faint end does not change significantly for each galaxy type.

As can be verified from figures 8, 9 and 10 these results are, in general, in very good agreement with what was found by other surveys such as the photometric MUSYC-ECDFS (Christlein et al. 2009) and COMBO-17 (Faber et al. 2007), as well as the spectroscopic VVDS (Zucca et al. 2006), DEEP-2 (Faber et al. 2007) and z-COSMOS (Zucca et al. 2009). In order to perform these compar-

isons we assumed that, in the MUSYC-ECDFS, early type galaxies correspond to our E-galaxies, while their late type objects (not shown because present large variations) correspond to our S-galaxies. Concerning the comparison with the VVDS, we assumed that their Type 1 galaxies correspond to our objects classified as E-type, while their Types 2 and 3 correspond to our S-types and their Type 4 corresponds to our (Irr+sb)-galaxies. When comparing with the DEEP-2 and COMBO-17 we assumed that their red galaxies represent our E-type galaxies and their blue sample represents our S-galaxies. The comparison with the z-COSMOS results was done assuming that their Type 1 corresponds to our E-galaxies, their Type 2 corresponds to our S-galaxies and their Types 3 and 4 correspond to our (Irr+sb) galaxies. Small discrepancies may have origin in the different criteria used to define the galaxy types in these works and in our analysis.

It is interesting to note that the lower panels of Figures 8 and 10 show that, in the range $z \approx 1.0 - 0.5$, most of the decline ϕ^* for the (Irr+sb)-type galaxies is compensated by a comparable increase of the E-type galaxies. This is consistent with the transformation of blue cloud galaxies into red sequence objects proposed by several previous authors (e.g., Bundy et al. 2006; Faber et al. 2007; Cattaneo et al. 2008; Stringer et al. 2009).

From table 6 we find that for $z \leq 0.2$ the rise of ϕ^* in the lower panel of Figure 6 is due to the contribution of the S and (Irr+sb) populations which is twice of that of the E-type galaxies, and which cause a decrease in the mean value of M^* . Even though this is a possible explanation, one should also be aware that in this interval photometric redshift errors are larger, in particular because the galaxy population is dominated by star-forming galaxies, which may impact the results.

We note that the good match between our results in the i' -band and those of other works concerning the evolutionary trends of M^* and ϕ^* is present even in the case of surveys in the B -band such as the DEEP-2 and z-COSMOS. In order to verify if the fact that we are comparing different bands introduces inconsistencies in this comparison (a younger stellar content predominantly contributes to the B -band while an older stellar content to the i' -band) we calculate the luminosity functions in a bluer filter such as the g' -band. The resulting M^* and ϕ^* are also plotted in figures 8, 9 and 10 and present a good agreement with the i' -band, indicating that the latter may be used to study the cosmic evolution of galaxy populations. We note that, when deriving the luminosity density evolution, Tresse et al. (2007) find measurable differences between the I and B bands in the VVDS data. Since, in our results, $M^*(z)$ is slightly steeper in the g' -band for latter types we checked for more subtle differences between the i' and g' bands performing linear fits to the M^* evolution for these filters, in the range $0.3 < z < 1.1$. The difference, in this redshift interval, is only 0.05 mag for the E-type galaxies and increases from ≈ 0.2 mag for the S-type galaxies to ≈ 0.4 mag for the (Irr+sb)-type galaxies. These results are consistent with a stronger evolution of the luminosity in the bluer bands, which probes star formation better, and is more intense in later type galaxies.

5. Conclusions

In this paper we have used the spectroscopic and photometric data available from VVDS and CFHTLS surveys to determine how well can we reproduce the evolution of luminosity function based on large photometric samples. This is a necessary exercise considering the large photometric surveys been planned for this decade.

Our main conclusions are:

1- Using a sample extracted from the VVDS data containing galaxies with both spectroscopic and photometric redshifts we obtain very similar luminosity functions, reproducing with z_{phot} the Schechter parameters M^* and ϕ^* obtained with z_{spec} , within the errorbars;

2- We also find that we can reproduce with the photometric data of the CFHTLS the evolution of M^* and ϕ^* of the spectroscopic VVDS sample as obtained by Ilbert et al. (2005). These results indicate from $z \approx 1.8$ to 0.3 a mild dimming in M^* of ≈ 0.7 mag while ϕ^* increases by a factor of ≈ 4 .

3- From the combined CFHTLS sample we estimate the cosmic variance in surveys areas ≈ 0.7 square degrees to be of order 0.15 in M^* and of order 25% in ϕ^* in the range $z = 0.3 - 1.3$;

4- The faint end slope of the global luminosity function varies from ≈ 1.5 to ≈ 1.3 from $z = 0.9$ to $z = 0.3$.

5- We used template fitting from the available Terapix photometric catalogs of the CFHTLS to assign galaxy types and derive type dependent luminosity functions. We find that we can reproduce with the combined CFHTLS sample the evolution of the characteristic parameters of the luminosity function of existing spectroscopic surveys such as the VVDS (Zucca et al. 2006), DEEP2 (Faber et al. 2007) and zCosmos (Zucca et al. 2009). Evolution of M^* , as a dimming with cosmic time, is similar for all galaxy types, but less pronounced for E-type galaxies. The characteristic densities ϕ^* of E and S type galaxies evolve similarly as an increase towards low redshifts, while very late types show a distinctive evolution with a decrease in density from $z = 1.2$ to 0.3.

6- We find also that the variation of the faint end slope of the global luminosity function is essentially due to the evolving mixture of galaxy types with the increasing proportion of E and S galaxy types with decreasing redshift.

There are issues in the present analysis that deserve further investigation with larger and deeper samples. For instance, the (Irr+sb)-type galaxies, which seem to play an important role at $z > 1.6$, are known to present large photometric redshift errors. A more detailed analysis involving the comparison with spectroscopic redshifts would be of interest to evaluate the reliability of the results obtained here.

Also, redefining the late-type sample, for instance by combining S+Irr as a single class and starburst galaxies as a separate class, may contribute to a better interpretation of the effects involved

in the evolution of the luminosity function and thus a better understanding of the processes driving galaxy evolution.

Finally, re-computing the photometric redshifts without the u^* -band may provide limits to the redshift interval which can be used to study the evolution of the luminosity function by future surveys such as DES that will not include this filter. Indeed Ilbert et al. (2006) show the importance of the u^* -band to photometric redshifts determinations in the ranges $z_{phot} < 0.4$ and $z_{phot} > 3$.

The results of this paper show the ability of photometric redshifts in estimating distances when a large database is used, as will be the case of DES and future projects in the Petabyte scale as LSST. Modern computational tools designed to treat this kind of data provide powerful analyzes taking advantage of multi-band photometry. Larger sky areas to be surveyed by these projects will yield deeper insight concerning the characterization of the galaxy luminosity function and its evolution.

Based on observations obtained with MegaPrime/MegaCam, a joint project of CFHT and CEA/DAPNIA, at the Canada-France-Hawaii Telescope (CFHT) which is operated by the National Research Council (NRC) of Canada, the Institut National des Science de l’Univers of the Centre National de la Recherche Scientifique (CNRS) of France, and the University of Hawaii. This work is based in part on data products produced at TERAPIX and the Canadian Astronomy Data Centre as part of the Canada-France-Hawaii Telescope Legacy Survey, a collaborative project of NRC and CNRS. This paper makes use of photometric redshifts produced jointly by Terapix and VVDS teams.

This research was carried out with the support of the Laboratório Interinstitucional de e-Astronomia (LIneA) operated jointly by the Centro Brasileiro de Pesquisas Físicas (CBPF), the Laboratório Nacional de Computação Científica (LNCC) and the Observatório Nacional (ON) and funded by the Ministério de Ciência e Tecnologia (MCT).

We thank an anonymous referee for useful comments that improved the paper. B.H.F.R. acknowledges financial support from the CNPq (DTI grant 381.358/09-7 associated with the PCI/MCT/ON Program). C.B. acknowledges the funding from the PCI/MCT-CBPF Program and the hospitality of ICRA-CBPF and ON, where part of this work was done. L.N.dC. acknowledges CNPq grants 476277 / 2006 and 304.202/2008-8, FAPERJ grants E-26/102.358/2009 and E-26/110.564/2010, and FINEP grants 01.06.0383.00 and 01.09.0298.00. A.A.M. acknowledges a fellowship from DS-CAPES Program.

REFERENCES

- Annis, J. 2000, <http://home.fnal.gov/~annis/astrophys/kcorr/sdss.kcorr.fits>
- Bañados, E., Hung, L., De Propris, R., & West, M. J. 2010, ApJ, 721, L14

- Benson, A. J., Bower, R. G., Frenk, C. S., Lacey, C. G., Baugh, C. M., & Cole, S. 2003, *ApJ*, 599, 38
- Blanton, M. R., Lupton, R. H., Schlegel, D. J., Strauss, M. A., Brinkmann, J., Fukugita, M., & Loveday, J. 2005, *ApJ*, 631, 208
- Blanton, M. R., et al. 2001, *AJ*, 121, 2358
- Bundy, K., et al. 2006, *ApJ*, 651, 120
- Cattaneo, A., Dekel, A., Faber, S. M., & Guiderdoni, B. 2008, *MNRAS*, 389, 567
- Cattaneo, A., Mamon, G. A., Warnick, K., & Knebe, A. 2010, *arXiv:1002.3257*
- Christlein, D., Gawiser, E., Marchesini, D., & Padilla, N. 2009, *MNRAS*, 400, 429
- Coleman, G. D., Wu, C.-C., & Weedman, D. W. 1980, *ApJS*, 43, 393
- Conselice, C. J. 2006, *ApJ*, 638, 686
- Croton, D. J., et al. 2005, *MNRAS*, 356, 1155
- Faber, S. M., et al. 2007, *ApJ*, 665, 265
- Fioc, M., & Rocca-Volmerange, B. 1997, *A&A*, 326, 950
- Folkes, S., et al. 1999, *MNRAS*, 308, 459
- Gabasch, A., et al. 2006, *A&A*, 448, 101
- Guzzo, L., et al. 2007, *ApJS*, 172, 254
- Ilbert, O., et al. 2005, *A&A*, 439, 863
- Ilbert, O., et al. 2006, *A&A*, 457, 841
- Iovino, A., et al. 2005, *A&A*, 442, 423
- Kinney, A. L., Calzetti, D., Bohlin, R. C., McQuade, K., Storchi-Bergmann, T., & Schmitt, H. R. 1996, *ApJ*, 467, 38
- Le Fèvre, O., et al. 2005, *A&A*, 439, 845
- Liu, C. T., Capak, P., Mobasher, B., Paglione, T. A. D., Rich, R. M., Scoville, N. Z., Tribiano, S. M., & Tyson, N. D. 2008, *ApJ*, 672, 198
- Madgwick, D. S., et al. 2002, *MNRAS*, 333, 133
- Marzke, R. O., & da Costa, L. N. 1997, *AJ*, 113, 185

- Marzke, R. O., da Costa, L. N., Pellegrini, P. S., Willmer, C. N. A., & Geller, M. J. 1998, *ApJ*, 503, 617
- Marzke, R. O., Huchra, J. P., & Geller, M. J. 1994, *ApJ*, 428, 43
- Montero-Dorta, A. D., & Prada, F. 2009, *MNRAS*, 399, 1106
- Oesch, P. A., et al. 2010, *ApJ*, 725, L150
- Reddy, N. A., & Steidel, C. C. 2009, *ApJ*, 692, 778
- Ryan, R. E., Jr., et al. 2007, *ApJ*, 668, 839
- Sandage, A., Binggeli, B., & Tammann, G. A. 1985, *AJ*, 90, 1759
- Schechter, P. 1976, *ApJ*, 203, 297
- Schmidt, M. 1968, *ApJ*, 151, 393
- Stringer, M. J., Benson, A. J., Bundy, K., Ellis, R. S., & Quetin, E. L. 2009, *MNRAS*, 393, 1127
- Trenti, M., Stiavelli, M., Bouwens, R. J., Oesch, P., Shull, J. M., Illingworth, G. D., Bradley, L. D., & Carollo, C. M. 2010, *ApJ*, 714, L202
- Tresse, L., et al. 2007, *A&A*, 472, 403
- Zucca, E., et al. 2006, *A&A*, 455, 879
- Zucca, E., et al. 2009, *A&A*, 508, 1217

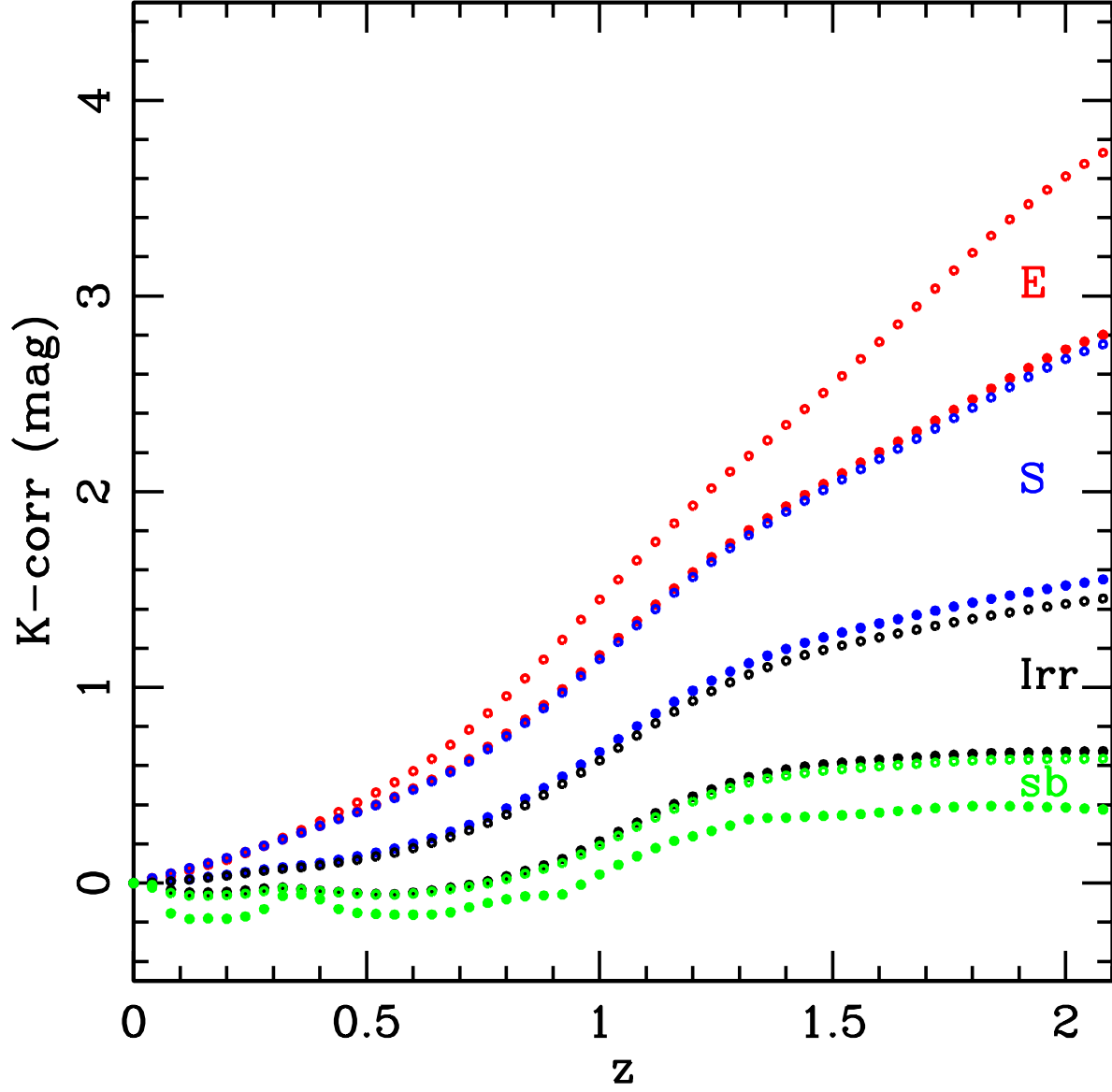


Fig. 1.— K -corrections for the i' -band for different galaxy types obtained from code Le Phare, where labels indicate the range of corrections for the 62 spectral types.

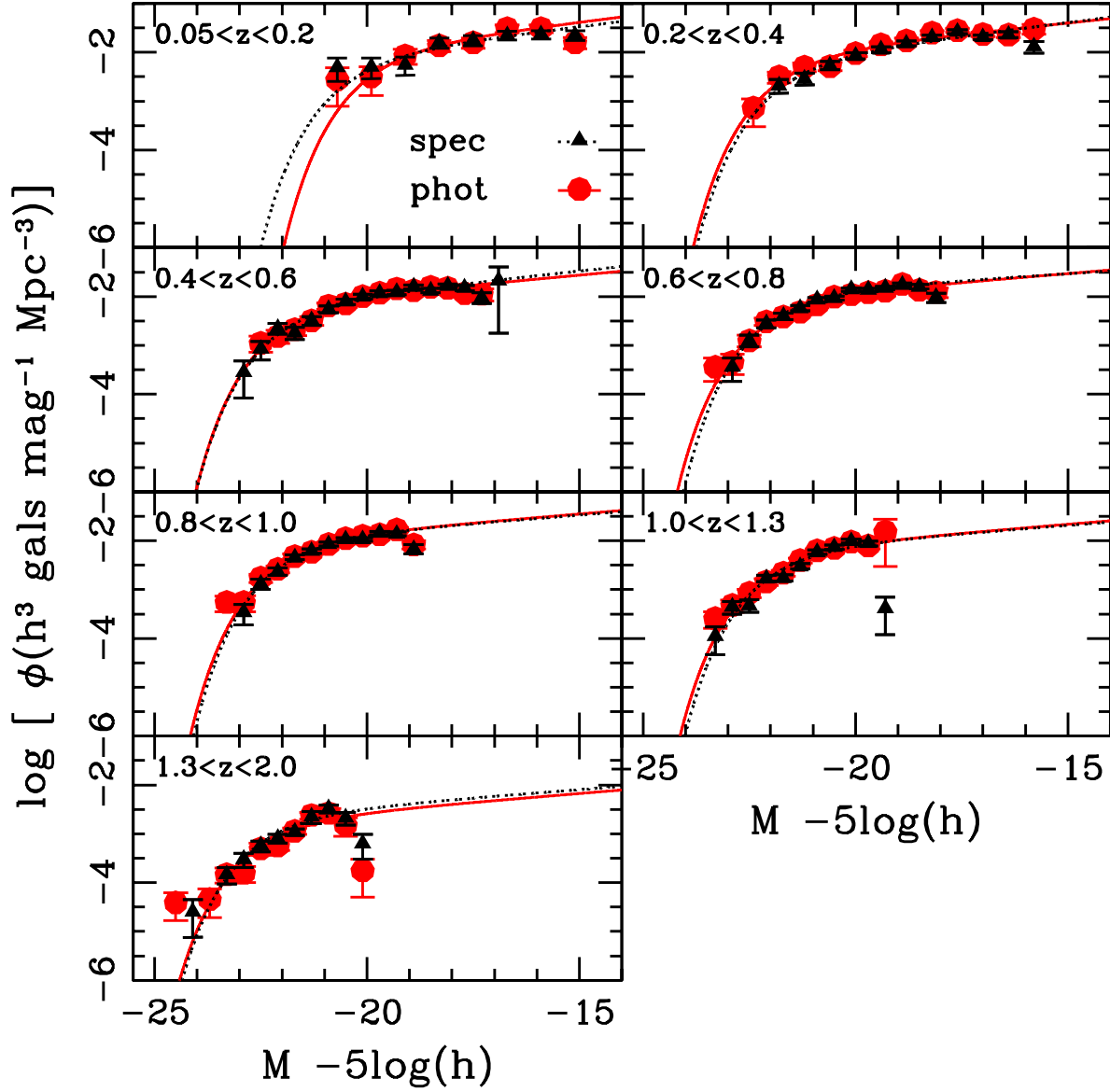


Fig. 2.— Luminosity functions in the i' -band for the Spectroscopic Sample in redshift bins. Black triangles and dashed lines represent the best spectroscopic data. Red dots and solid lines show the function determined with photometric redshifts.

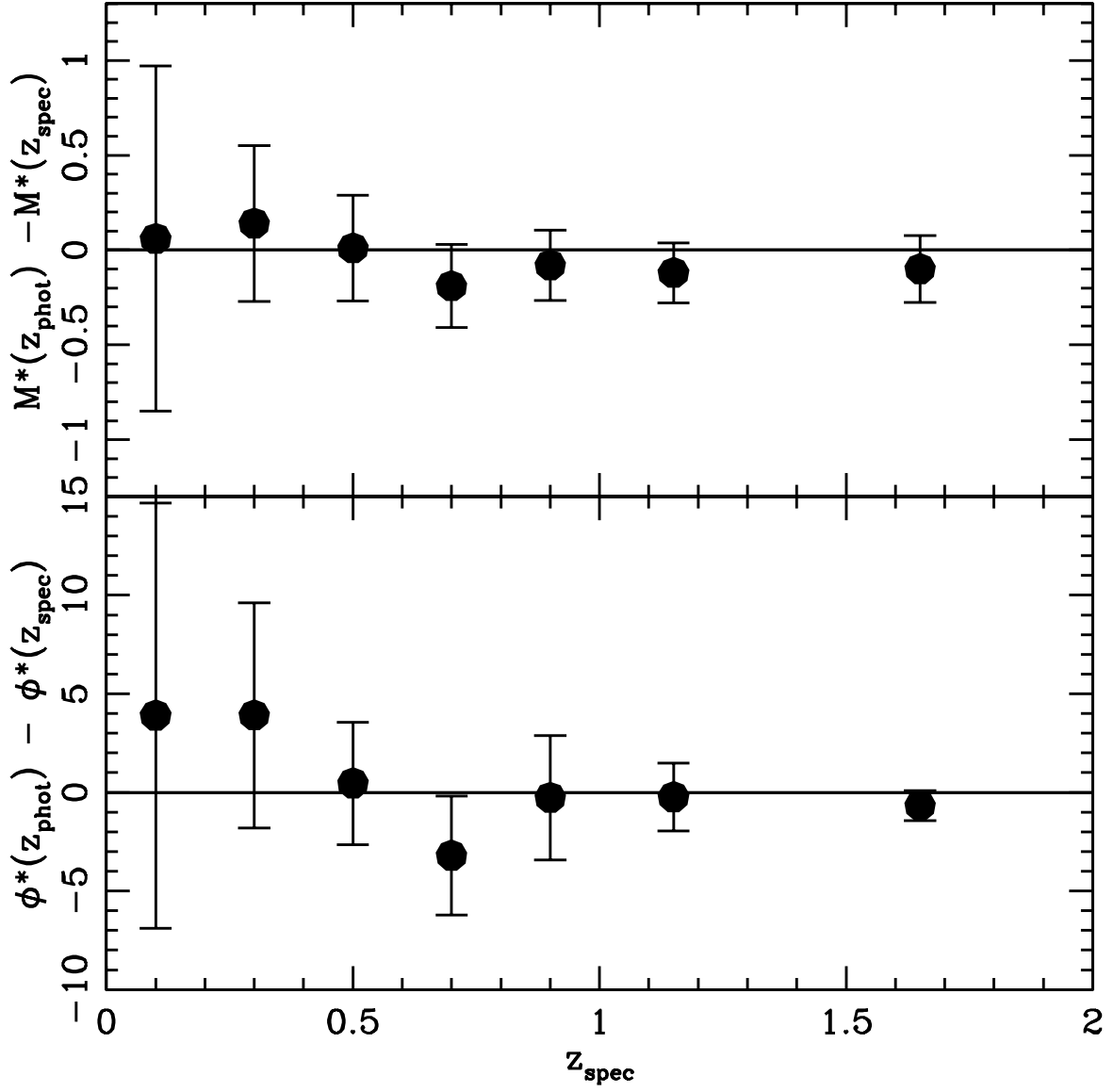


Fig. 3.— Comparison of M^* (upper panel) and ϕ^* (lower panel) for luminosity functions derived with z_{spec} and z_{phot} data for the Spectroscopic Sample. Units for the differences of M^* and ϕ^* are mag and $10^{-3}h^3\text{gals mag}^{-1}\text{Mpc}^{-3}$ respectively.

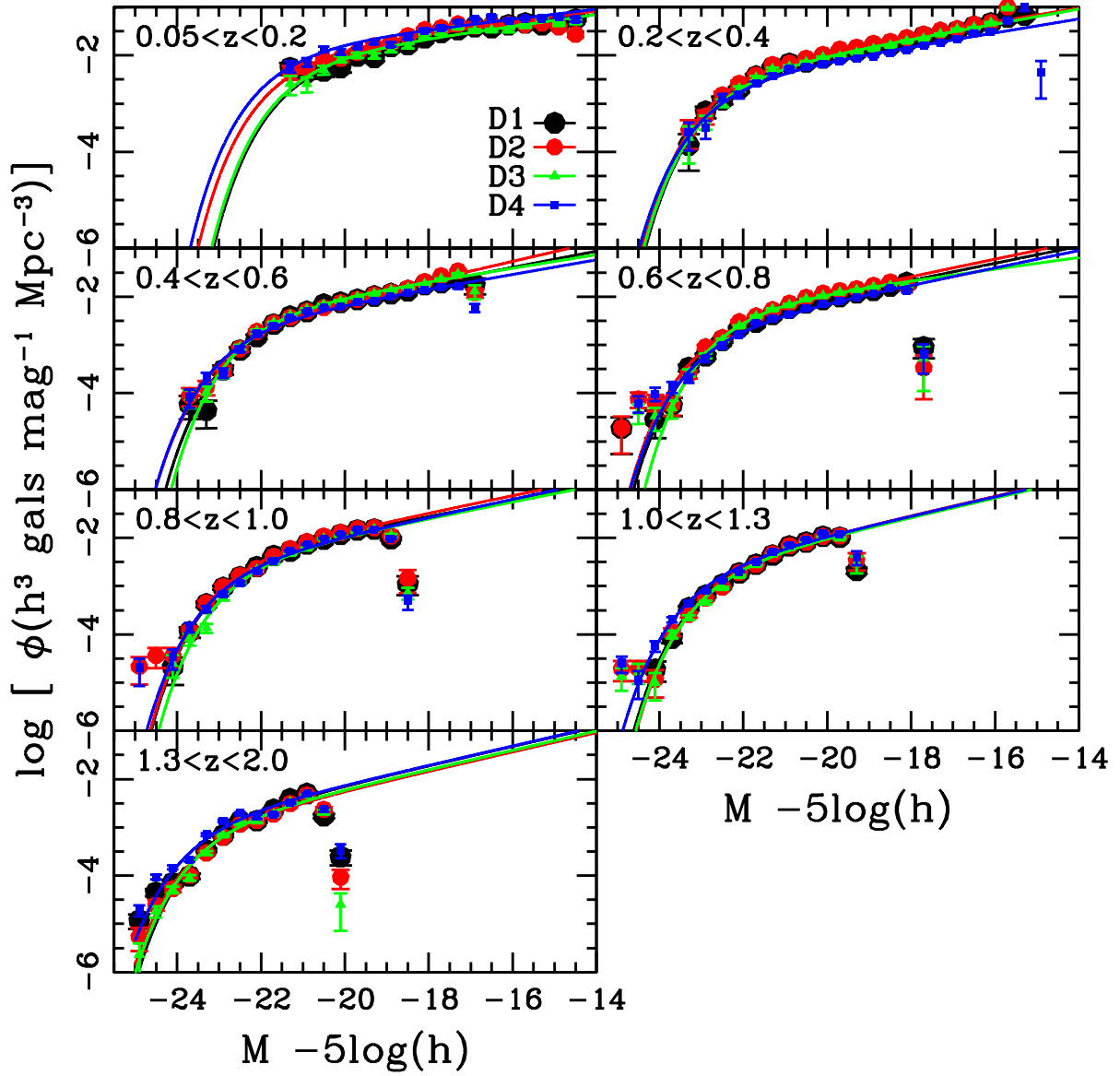


Fig. 4.— Luminosity functions in the i' -band for the four CFHTLS fields and their Schechter fits.

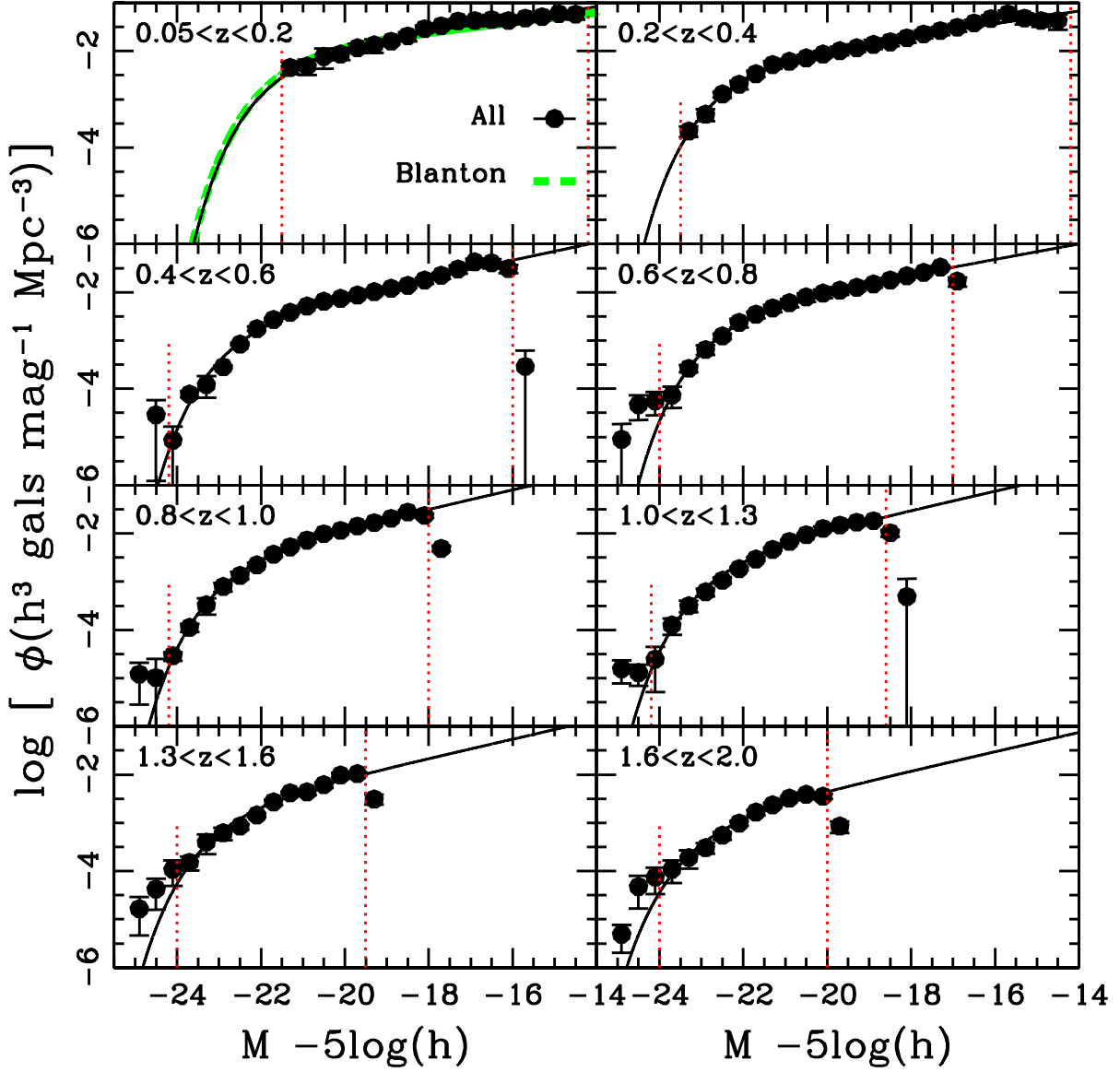


Fig. 5.— Luminosity functions in the i' -band and Schechter fits for the combined CFHTLS areas. Red dotted vertical lines indicate the limits where the fits were performed. The fit obtained by Blanton et al. (2001) for the SDSS is shown with a green dot-dashed line in the upper left panel.

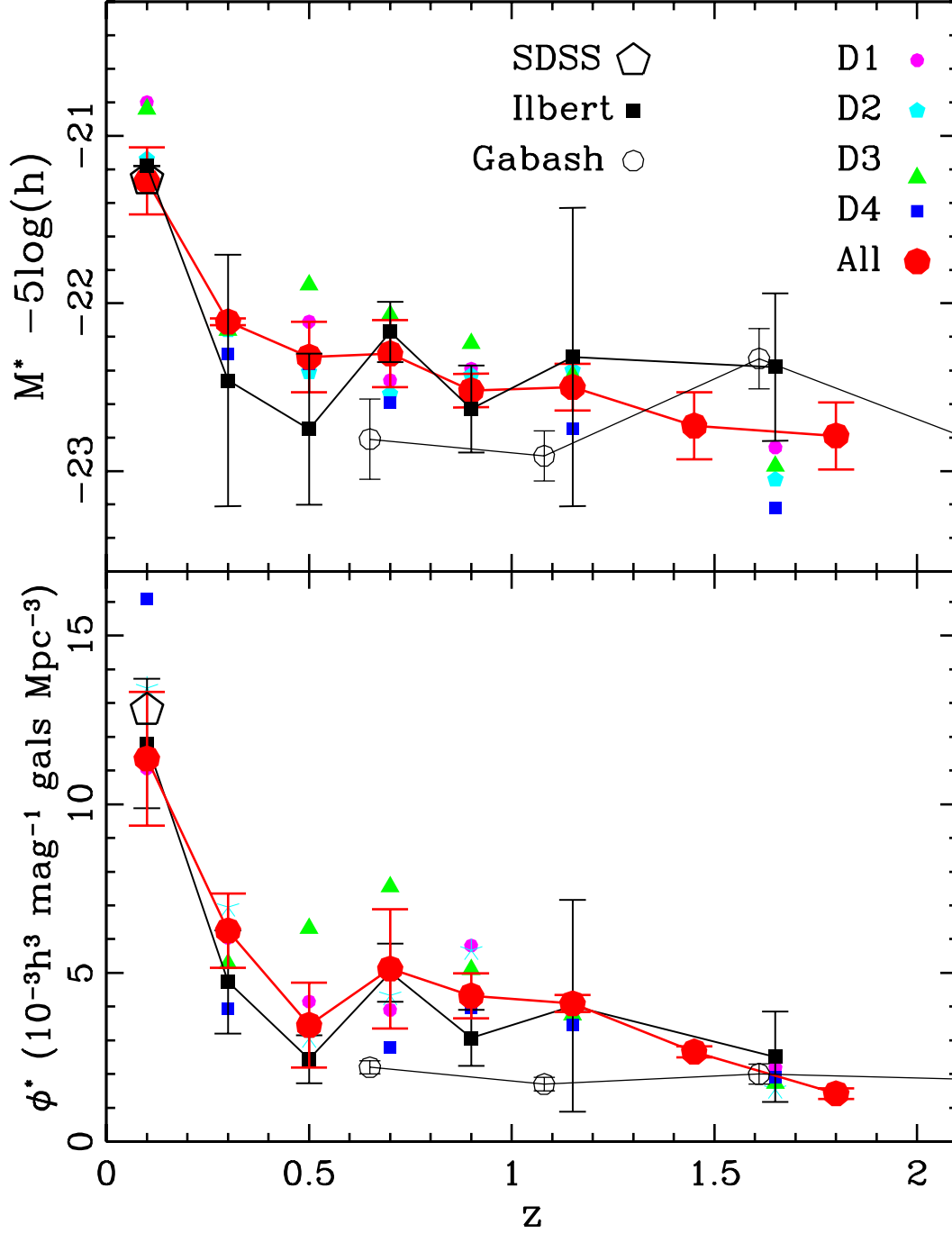


Fig. 6.— Evolution of M^* and ϕ^* for the combined CFHTLS areas (red dots). Error bars are the square root of the variances from the four individual CFHTLS fields. The results obtained by Ilbert et al. (2005) are shown as black squares, by Blanton et al. (2001) for SDSS as a black open pentagon and by Gabasch et al. (2006) as black open circles.

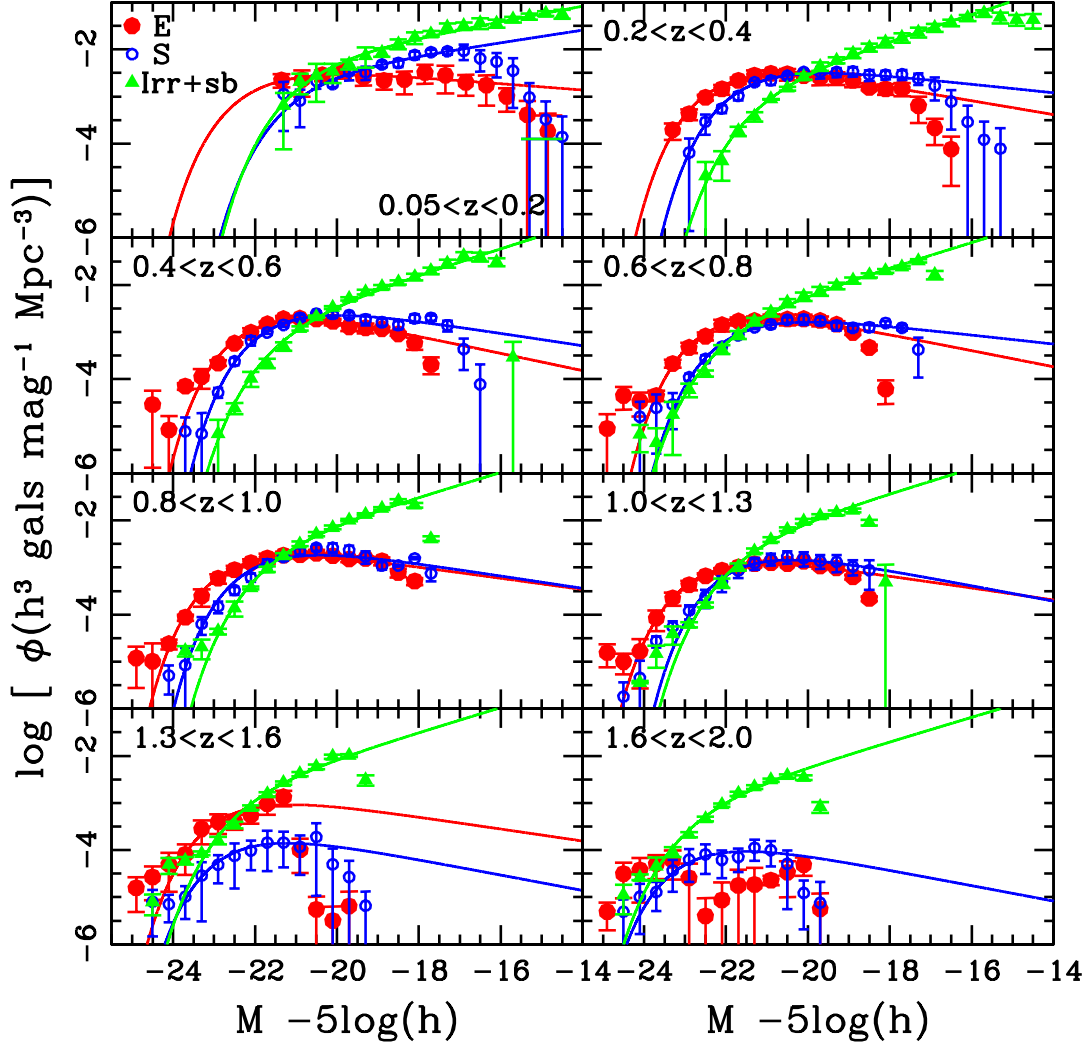


Fig. 7.— Luminosity functions in the i' -band and Schechter fits for the combined CFHTLS areas. E-type galaxies are shown with red dots, S-type galaxies with blue open circles and (Irr+sb)-type with green triangles.

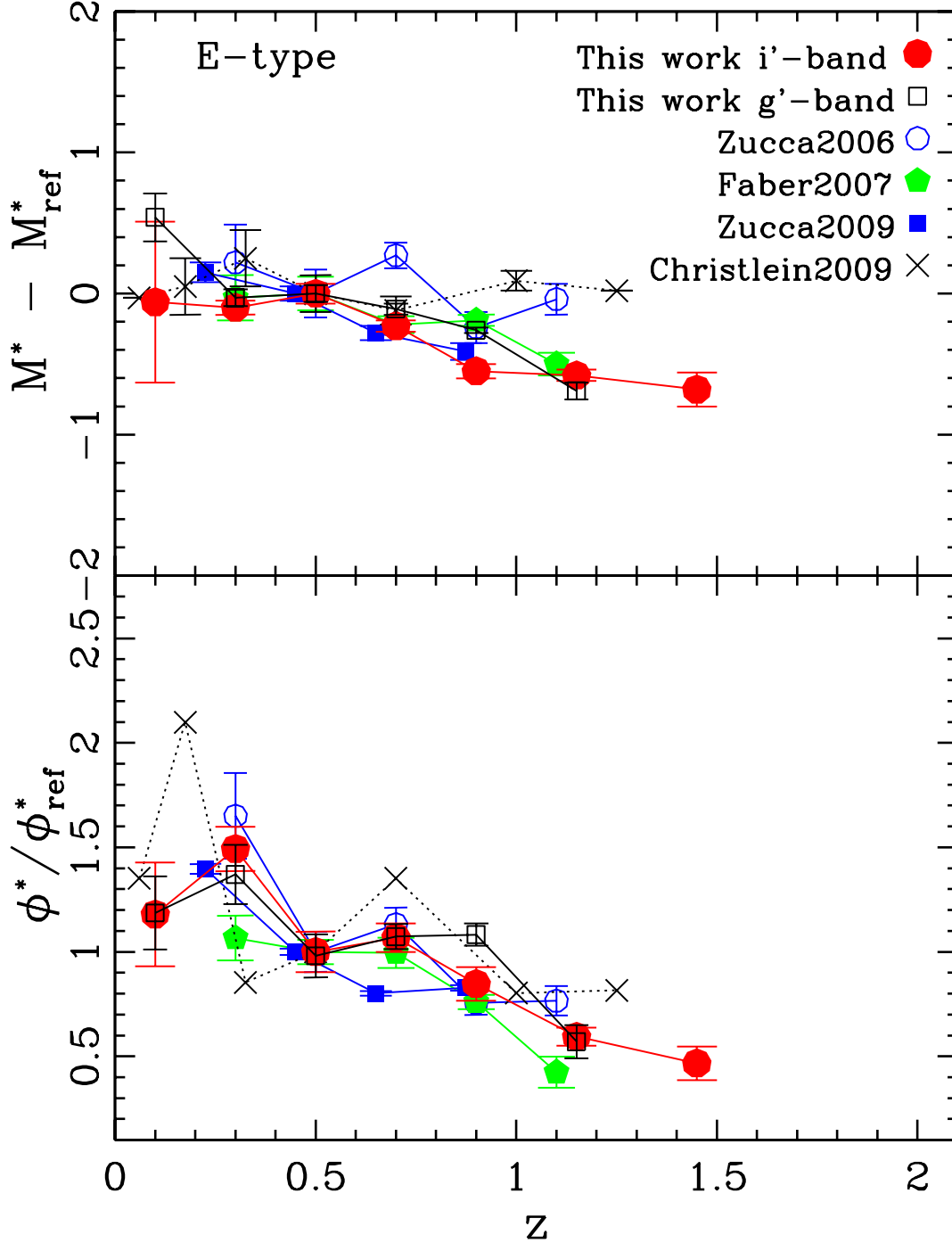


Fig. 8.— Evolution of M^* (upper panel) and ϕ^* (lower panel) for E-type galaxies of the combined CFHTLS areas in the i' -band (red dots) and in the g' -band (black empty squares). Results are shown with reference to those at $z = 0.5$. Results from other surveys are presented with symbols shown in the upper panel.

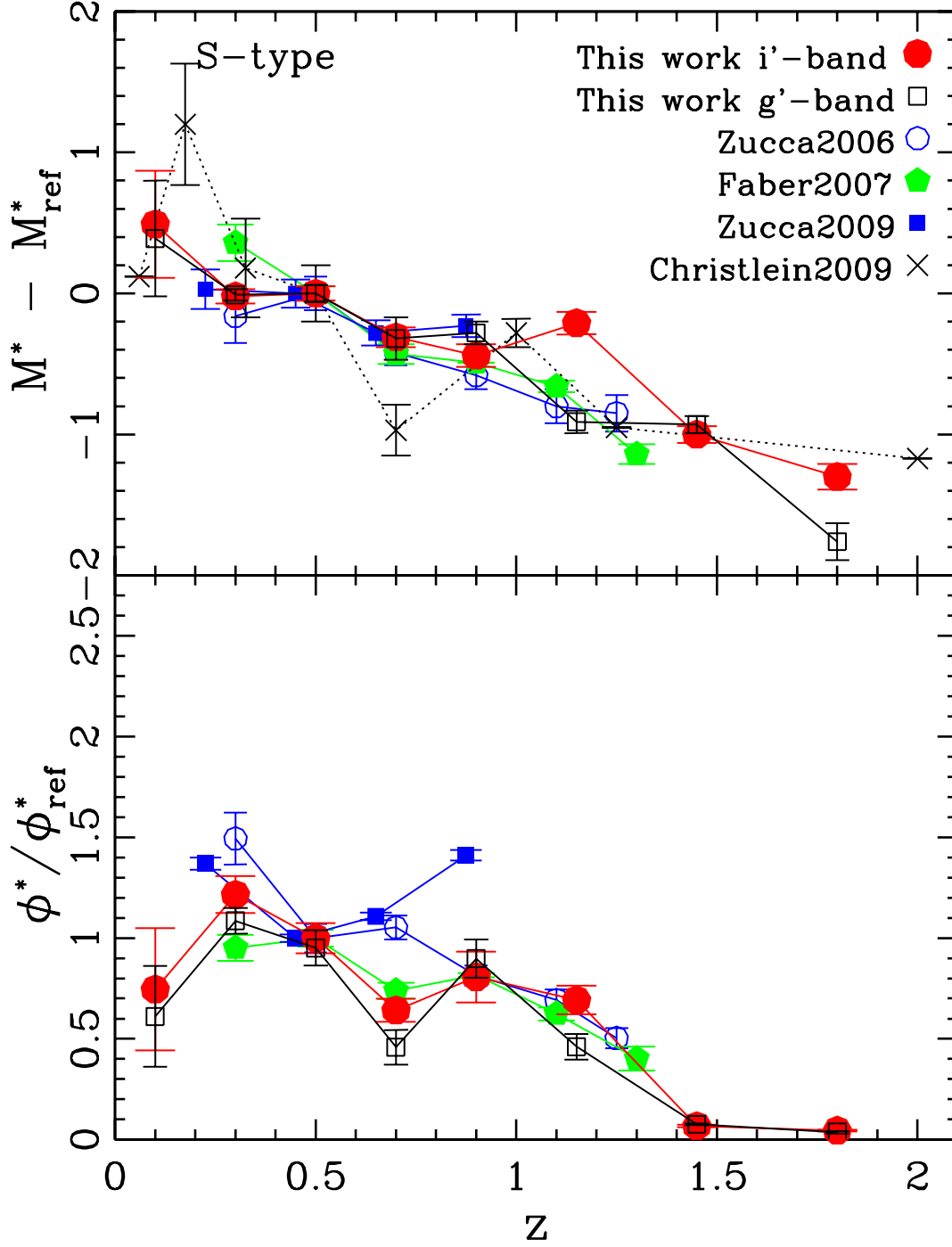


Fig. 9.— Evolution of M^* (upper panel) and ϕ^* (lower panel) for S-type galaxies of the combined CFHTLS areas in the i' -band (red dots) and in the g' -band (black empty squares). Results are shown with reference to those at $z = 0.5$. Results from other surveys are presented with symbols shown in the upper panel.

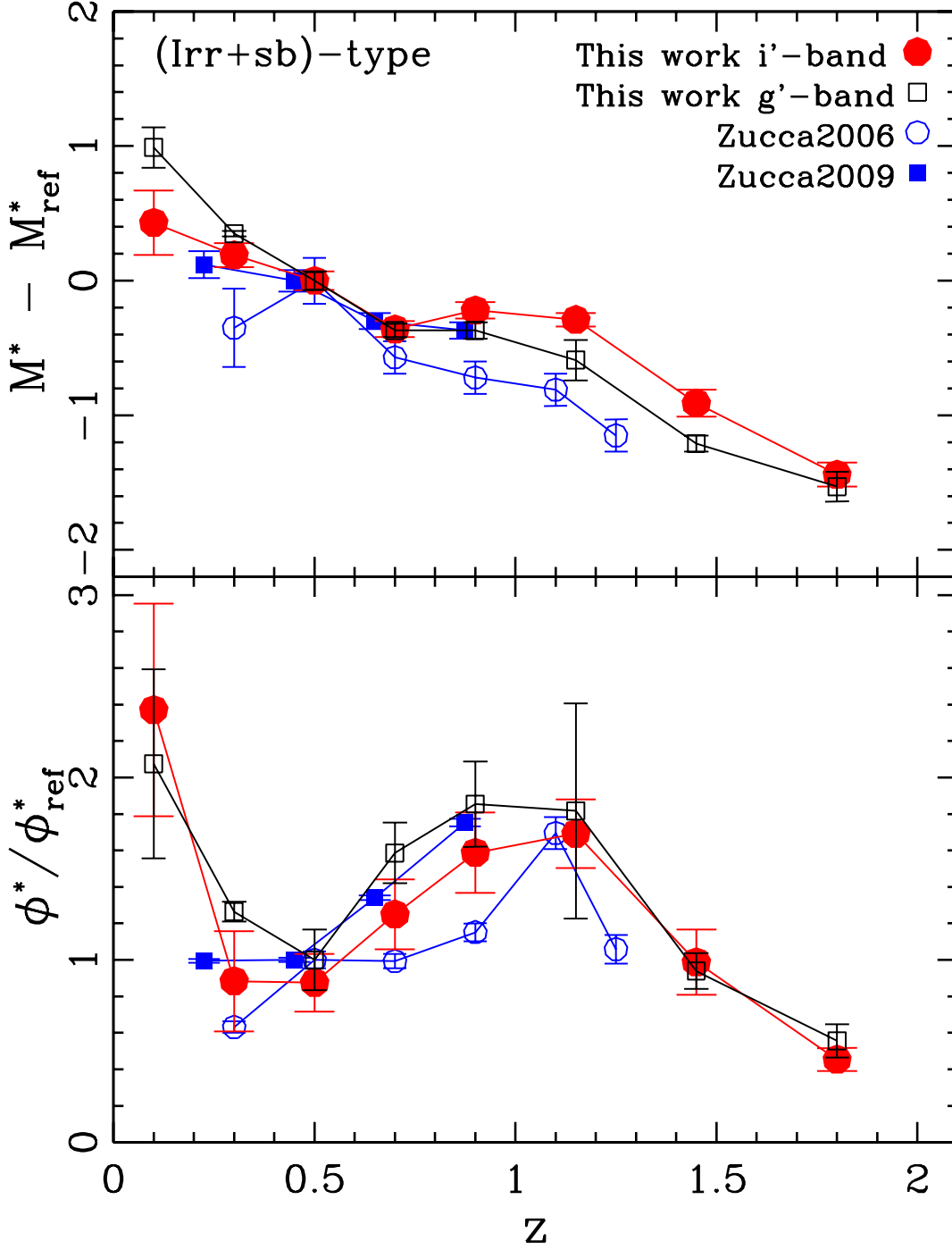


Fig. 10.— Evolution of M^* (upper panel) and ϕ^* (lower panel) for (Irr+sb)-type galaxies of the combined CFHTLS areas in the i' -band (red dots) and in the g' -band (black empty squares). Results are shown with reference to those at $z = 0.5$. Results from other surveys are presented with symbols shown in the upper panel.

Table 1. Properties of CFHTLS Deep fields.

Field	RA	DEC	u^*	g'	r'	i'	z'	Eff.Area
(1)	(J2000) (2)	(J2000) (3)	(4)	(5)	(6)	(7)	(8)	(deg ²) (9)
D1	02:25:59	-04:29:40	26.5	26.4	26.1	25.9(25.1)	25.0	0.71
D2	10:00:28	+02:12:30	26.1	26.2	26.0	25.7(24.9)	24.9	0.69
D3	14:19:27	+52:40:56	25.9	26.6	26.4	26.2(25.7)	25.1	0.80
D4	22:15:31	-17:43:56	26.5	26.3	26.4	26.0(25.3)	25.0	0.74

Note. — Col. (1): Field name. Col. (2) and (3): Central position of the field (RA presented in hours, minutes and seconds, and DEC in degrees, arc minutes and arc seconds). Col. (4)-(8): Completeness magnitude (50%, AB) of each band (for the i' band we also show the 80% completeness magnitude inside parenthesis). Col. (9): Effective area (which exclude masked regions) in square degrees.

Table 2. Galaxy distribution with redshift.

Δz (1)	SS (2)	D1 (3)	D2 (4)	D3 (5)	D4 (6)	E (7)	S (8)	Irr+sb (9)	Tot (10)
0.05-0.2	201	2346	2481	2549	3390	722	1569	11174	13465
0.2-0.4	721	7327	8616	8452	5515	3762	4698	36903	45363
0.4-0.6	784	7345	7934	9242	6541	4633	6636	44617	55886
0.6-0.8	1043	8483	10364	11218	7320	7501	7374	48798	63673
0.8-1.0	1082	9314	9875	9534	9584	9096	10907	51569	71572
1.0-1.3	708	7497	7541	8240	9508	8598	11568	55710	75876
1.3-2.0	274	5022	4200	5073	5470
1.3-1.6	3130	1046	31928	36104
1.6-2.0	453	924	22594	23971

Note. — Col. (1): Redshift bin. Col. (2): Spectroscopic Sample. Col. (3)-(6): CFHTLS fields. Col. (7)-(9): Subsamples of galaxy types. Col. (10): Combined data of the four fields. Columns (2)-(6) refer to samples with limits $17.5 \leq i'_{AB} \leq 24$ and $z_{phot} \leq 2.0$. Columns (7)-(10) refer to samples with limits $17.5 \leq i'_{AB} \leq 25$ and $z_{phot} \leq 2.5$.

Table 3. Schechter function parameters for the Spectroscopic Sample.

$\langle z \rangle$ (1)	M^* (mag-5log(h)) (2)	ϕ^* ($10^{-3}h^3\text{gals mag}^{-1}\text{Mpc}^{-3}$) (3)	α (4)
<i>z_{spec}</i>			
0.10	-20.17 \pm 1.10	10.07 \pm 9.57	-1.27 \pm 0.21
0.30	-21.44 \pm 0.31	8.40 \pm 2.74	-1.28 \pm 0.07
0.50	-21.71 \pm 0.14	8.22 \pm 1.75	-1.24 \pm 0.07
0.70	-21.65 \pm 0.11	13.53 \pm 1.91	-1.14 \pm 0.06
0.90	-21.70 \pm 0.15	12.74 \pm 2.44	-1.17 \pm 0.10
1.15	-21.69 \pm 0.13	7.87 \pm 1.48	-1.17
1.65	-22.16 \pm 0.12	2.85 \pm 0.53	-1.17
<i>z_{phot}</i>			
0.10	-19.59 \pm 0.37	14.40 \pm 6.11	-1.27 \pm 0.12
0.30	-21.47 \pm 0.20	10.98 \pm 2.98	-1.23 \pm 0.07
0.50	-21.70 \pm 0.24	8.68 \pm 2.56	-1.20 \pm 0.10
0.70	-21.84 \pm 0.19	10.33 \pm 2.34	-1.18 \pm 0.08
0.90	-21.78 \pm 0.11	12.47 \pm 2.02	-1.18 \pm 0.09
1.15	-21.81 \pm 0.09	7.64 \pm 0.88	-1.18
1.65	-22.26 \pm 0.13	2.18 \pm 0.54	-1.18

Note. — Col. (1): Central value of redshift interval. Col. (2): Characteristic absolute magnitude and its Poisson error. Col. (3): Characteristic density and its Poisson error. Col. (4): Faint-end slope and its Poisson error (for $z \geq 1.0$ it is fixed to -1.17 and -1.18 when using z_{spec} and z_{phot} , respectively).

Table 4. Schechter function parameters for the CFHTLS fields.

$< z >$ (1)	M^* (mag-5log(h)) (2)	ϕ^* ($10^{-3}h^3\text{gals mag}^{-1}\text{Mpc}^{-3}$) (3)	α (4)
D1			
0.10	-20.80 ± 0.30	11.06 ± 2.93	-1.31 ± 0.05
0.30	-22.10 ± 0.07	6.04 ± 0.65	-1.38 ± 0.02
0.50	-22.11 ± 0.14	4.15 ± 1.15	-1.42 ± 0.05
0.70	-22.46 ± 0.07	3.90 ± 0.60	-1.44 ± 0.03
0.90	-22.39 ± 0.03	5.81 ± 0.40	-1.41 ± 0.08
1.15	-22.47 ± 0.03	3.87 ± 0.23	-1.50
1.65	-22.86 ± 0.10	2.20 ± 0.38	-1.50
D2			
0.10	-21.14 ± 0.29	13.45 ± 3.52	-1.29 ± 0.05
0.30	-22.16 ± 0.04	6.95 ± 0.48	-1.36 ± 0.02
0.50	-22.41 ± 0.13	3.06 ± 0.74	-1.50 ± 0.08
0.70	-22.54 ± 0.15	4.33 ± 1.35	-1.45 ± 0.16
0.90	-22.43 ± 0.08	5.67 ± 0.77	-1.45 ± 0.04
1.15	-22.40 ± 0.04	4.14 ± 0.35	-1.50
1.65	-23.05 ± 0.00	1.55 ± 0.25	-1.50
D3			
0.10	-20.84 ± 0.21	11.50 ± 2.45	-1.30 ± 0.04
0.30	-22.16 ± 0.06	5.28 ± 0.46	-1.39 ± 0.02
0.50	-21.89 ± 0.05	6.32 ± 0.61	-1.35 ± 0.04
0.70	-22.07 ± 0.03	7.55 ± 0.47	-1.30 ± 0.03
0.90	-22.24 ± 0.13	5.10 ± 1.30	-1.43 ± 0.11
1.15	-22.43 ± 0.07	3.76 ± 0.42	-1.50
1.65	-22.97 ± 0.08	1.73 ± 0.28	-1.50
D4			
0.10	-21.29 ± 0.32	16.08 ± 4.07	-1.26 ± 0.04
0.30	-22.30 ± 0.11	3.94 ± 0.61	-1.36 ± 0.03
0.50	-22.36 ± 0.10	3.38 ± 0.61	-1.38 ± 0.04
0.70	-22.59 ± 0.11	2.79 ± 0.49	-1.45 ± 0.05
0.90	-22.57 ± 0.12	3.98 ± 0.96	-1.47 ± 0.08
1.15	-22.75 ± 0.04	3.45 ± 0.26	-1.50
1.65	-23.22 ± 0.25	1.90 ± 0.52	-1.50

Note. — The meanings of columns are the same as in Table 3. The value of α for $z \geq 1.0$ is fixed to -1.50.

Table 5. Schechter function parameters for the combined CFHTLS fields.

$< z >$	M^*	ϕ^*	α
(1)	(mag-5log(h))	($10^{-3}h^3$ gals $\text{mag}^{-1}\text{Mpc}^{-3}$)	(4)
0.10	-21.28 ± 0.26	11.24 ± 2.44	-1.31 ± 0.03
0.30	-22.11 ± 0.07	6.22 ± 0.64	-1.34 ± 0.02
0.50	-22.31 ± 0.06	3.47 ± 0.49	-1.46 ± 0.03
0.70	-22.30 ± 0.02	5.12 ± 0.22	-1.40 ± 0.01
0.90	-22.52 ± 0.04	4.32 ± 0.39	-1.50 ± 0.02
1.15	-22.48 ± 0.05	4.16 ± 0.32	-1.50
1.45	-22.73 ± 0.09	2.63 ± 0.31	-1.50
1.80	-22.76 ± 0.11	1.49 ± 0.23	-1.50

Note. — The meanings of columns are the same as in Table 3. The value of α for $z \geq 1.0$ is fixed to -1.50.

Table 6. Schechter function parameters for the combined CFHTLS fields separated by galaxy type.

$\langle z \rangle$	M^* (mag-5log(h))	ϕ^* ($10^{-3}h^3\text{gals mag}^{-1}\text{Mpc}^{-3}$)	α
(1)	(2)	(3)	(4)
E-type			
0.10	-21.73 ± 0.57	5.00 ± 1.05	-0.83 ± 0.08
0.30	-21.77 ± 0.05	6.33 ± 0.45	-0.63 ± 0.04
0.50	-21.67 ± 0.07	4.24 ± 0.41	-0.54 ± 0.06
0.70	-21.90 ± 0.04	4.53 ± 0.29	-0.57 ± 0.04
0.90	-22.22 ± 0.05	3.59 ± 0.34	-0.70 ± 0.05
1.15	-22.25 ± 0.04	2.52 ± 0.18	-0.68 ± 0.04
1.45	-22.35 ± 0.12	1.98 ± 0.34	-0.68
S-type			
0.10	-20.68 ± 0.38	3.66 ± 1.49	-1.33 ± 0.11
0.30	-21.19 ± 0.05	5.97 ± 0.45	-0.77 ± 0.03
0.50	-21.17 ± 0.05	4.91 ± 0.37	-0.67 ± 0.04
0.70	-21.48 ± 0.07	3.15 ± 0.28	-0.76 ± 0.04
0.90	-21.61 ± 0.08	3.96 ± 0.62	-0.67 ± 0.08
1.15	-21.38 ± 0.08	3.40 ± 0.35	-0.59 ± 0.07
1.45	-22.17 ± 0.06	0.33 ± 0.03	-0.59
1.80	-22.47 ± 0.09	0.22 ± 0.02	-0.59
(Irr+sb)-type			
0.10	-20.55 ± 0.13	7.58 ± 1.33	-1.41 ± 0.03
0.30	-20.97 ± 0.07	2.44 ± 0.36	-1.70 ± 0.04
0.50	-21.16 ± 0.07	2.40 ± 0.43	-1.69 ± 0.05
0.70	-21.76 ± 0.07	2.47 ± 0.36	-1.67 ± 0.07
0.90	-21.45 ± 0.08	4.34 ± 0.75	-1.65 ± 0.06
1.15	-21.50 ± 0.12	4.84 ± 1.17	-1.66 ± 0.10
1.45	-22.09 ± 0.24	2.85 ± 0.40	-1.66
1.80	-22.55 ± 0.24	1.42 ± 0.17	-1.66

Note. — The meanings of columns are the same as in Table 3. The value of α for $z \geq 1.3$ is fixed to that obtained in the previous redshift bin.